International Journal of Thermal Sciences 49 (2010) 281–289

Contents lists available at ScienceDirect

International Journal of Thermal Sciences

journal homepage: www.elsevier.com/locate/ijts

# Pressure-driven water flow through carbon nanotubes: Insights from molecular dynamics simulation

John A. Thomas, Alan J. H. McGaughey*, Ottoleo Kuter-Arnebeck

*Department of Mechanical Engineering, Carnegie Mellon University, Pittsburgh, PA 15213, USA*

ARTICLE INFO

*Article history:*
Received 23 April 2009
Received in revised form
8 July 2009
Accepted 9 July 2009
Available online 31 July 2009

*Keywords:*
Molecular dynamics simulation
Water flow
Slip flow
Carbon nanotubes (CNT)
Carbon nanopipes

ABSTRACT

Pressure-driven water flow through carbon nanotubes (CNTs) is examined using molecular dynamics simulation. The results are compared to reported experimental flow rate measurements through similarly sized CNTs and larger carbon nanopipes. By using molecular dynamics simulation to predict the variation of water viscosity and slip length with CNT diameter, we find that flow through CNTs with diameters as small as 1.66 nm can be fully understood using continuum fluid mechanics. Potential mechanisms to explain the differences between the flow rates predicted from simulation and those measured in experiments are identified and discussed.



## 1. Introduction and background

Reports of new techniques for growing straight and axially-aligned carbon nanotubes (CNTs) and carbon nanopipes with controllable lengths and diameters have generated interest in nanofluidic devices [1–8]. Open-ended CNT membranes, which are formed by filling the interstitial region between 1 and 10 nm diameter CNTs with a non-porous matrix material, have been proposed as next-generation desalination [9,10], gas separation [11], and gas storage devices [12]. Carbon nanopipe bundles, which are formed by depositing carbon on the pore walls of a removable molding template, are currently being tested as hypodermic drug-delivery needles [6] and cellular probes [13]. Despite these advances in fabrication capabilities and new insight into the mechanism of gas transport through CNTs [14], the nature of pressure-driven liquid flow through CNTs and carbon nanopipes is not clear [15].

The measured flow rates of glycerine and water through carbon nanopipes with diameters larger than 200 nm are consistent with predictions from the no-slip Poiseuille flow relation [7]. For 44 nm diameter carbon nanopipes, 7 nm diameter CNTs, and 1.6 nm diameter CNTs, the experimentally measured water flow rates exceed predictions from the no-slip Poiseuille flow relation by up to several orders of magnitude [2–4]. Results from molecular dynamics (MD) simulations suggest that flow enhancement in CNTs is caused by liquid slip at the water/carbon boundary and confinement-related changes in the liquid viscosity [16–19]. The precise magnitude of this enhancement, however, is unknown and the variations in viscosity and slip length with diameter are not fully understood.

In a previous work, we used MD simulation to study water flow in CNTs with diameters between 4.99 nm and 1.66 nm [19]. We predicted the variation in flow enhancement with CNT diameter and identified how it is related to the water viscosity and the water/CNT slip length. We found that liquid flow through CNTs with diameters as small as 1.66 nm can be described using the slip-modified Poiseuille relation. In this report, we discuss in more detail the available experimental data and present our findings in the context of more recent flow measurements. We expand on our previous work by providing additional insights into the structure and thermophysical properties of water confined inside CNTs, and propose additional mechanisms to account for the differences between experimental flow measurements and those predicted from simulations.

We begin in Sections 2 and 3 with a review of the Poiseuille flow relation and a summary of the available experimental flow enhancement data. Next, in Section 4, we introduce MD simulation, discuss the structure of water inside CNTs, and describe how water

* Corresponding author.
*E-mail address:* mcgaughey@cmu.edu (A.J.H. McGaughey).

1290-0729/$ – see front matter © 2009 Elsevier Masson SAS. All rights reserved.
doi:10.1016/j.ijthermalsci.2009.07.008

molecules interact with the CNT surface. In Section 5, we review the available simulation flow data and discuss how MD simulation can be used to evaluate the water/carbon slip length and the viscosity of water inside CNTs. In Section 6, we discuss the flow enhancements predicted from MD simulation in the context of the experimental measurements. We conclude in Section 7 with a discussion of the future research needed in this area.

## 2. Pressure-driven liquid flow

When subjected to an axial pressure gradient, $\partial P/\partial z$, the radial velocity profile, $u(r)$, of an incompressible liquid creeping (Reynolds number much less than one) steadily through a tube of radius $R$ is

$$u(r) = \frac{R^2}{4\mu}\left[1 - \frac{r^2}{R^2} + \frac{2L_s}{R}\right]\frac{\partial P}{\partial z}, \tag{1}$$

where $\mu$ is the liquid viscosity and $L_s$ is the slip length at the liquid/solid boundary. The slip length, which describes the velocity discontinuity between the liquid and the solid, is typically defined as [20,21].

$$L_s \equiv \left.\frac{u(r)}{\mathrm{d}u/\mathrm{d}r}\right|_{r=R}. \tag{2}$$

Predictions from MD simulation indicate that Eq. (1) (the Poiseuille parabola) is valid when the characteristic flow diameter is 5–10 times larger than the characteristic molecular diameter ($\approx$0.17 nm for water) [22,23]. In smaller systems, where the continuum approximation is invalid, molecular transport is governed by the liquid structure and collective molecular motion [24–26].

In Fig. 1, we show how liquid slip at the solid/liquid boundary affects the velocity profile inside the tube. When $L_s = 0$, the liquid velocity at the wall is zero and the maximum velocity (at the tube centerline) is twice the mean flow velocity. With increasing slip length, the mean flow velocity increases, the relative difference between the maximum and minimum velocities decreases, and the velocity profile becomes more plug-like [27]. The velocity of the liquid at the solid surface can also be quantified using the slip coefficient, $L_c$. As shown in Fig. 1, the slip coefficient is the difference between the radial position at which the velocity profile would become zero and the radial position of the solid surface [28]. For linear velocity profiles, (*e.g.* boundary-driven Couette flow), the slip length and slip coefficient are equal. These values are different for Poiseuille flow.

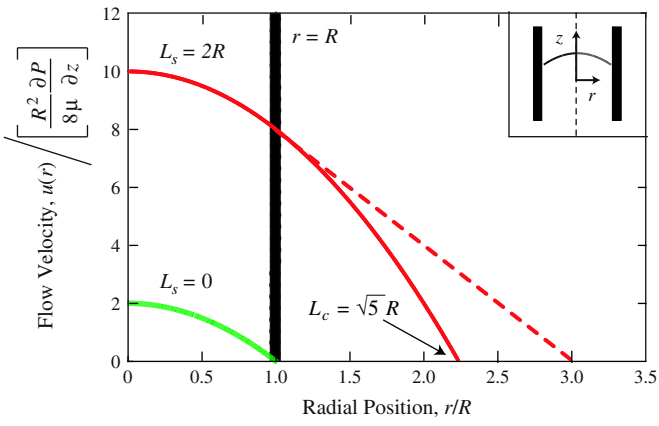


**Fig. 1.** No-slip Poiseuille flow ($L_s = 0$) and slip Poiseuille flow with $L_s = 2R$ through a tube with radius $R$. The thick vertical lines indicate the location of the tube wall. The slip coefficient for the slip system, $L_c$, is $\sqrt{R^2 + 2RL_s} = \sqrt{5}R$. The flow velocity is normalized by the mean velocity corresponding to no-slip flow.

The volumetric flow rate with slip, $Q_S$, is found by integrating the velocity profile over the tube cross-section [29]:

$$Q_S = \int_0^R u(r)2\pi r\,\mathrm{d}r = \frac{\pi\left[(d/2)^4 + 4(d/2)^3 L_s\right]}{8\mu}\frac{\partial P}{\partial z}, \tag{3}$$

where $d(= 2R)$ is the tube diameter. Equation (3) is the slip-modified Poiseuille flow rate; the no-slip Poiseuille flow rate, $Q_N$, is found by setting $L_s$ equal to zero.

The flow rate enhancement, $\varepsilon$, is defined as the ratio of the actual flow rate, $Q_A$, to $Q_N$:

$$\varepsilon \equiv \frac{Q_A}{Q_N}. \tag{4}$$

If the actual flow is modeled using Eq. (3), such that $Q_A = Q_S$, the enhancement factor is:

$$\varepsilon = \left[1 + 8\frac{L_s(d)}{d}\right], \tag{5}$$

where $L_s(d)$ is the diameter-dependent slip length. In addition to liquid slip, however, diameter-related changes in the fluid viscosity may affect the flow [30,31]. If $Q_N$ is calculated using the bulk liquid viscosity, $\mu_\infty$, then the diameter-specific fluid viscosity, $\mu(d)$, can be incorporated into Eq. (5) such that

$$\varepsilon = \left[1 + 8\frac{L_s(d)}{d}\right]\frac{\mu_\infty}{\mu(d)}. \tag{6}$$

## 3. Experimental measurements

### 3.1. Water flow through carbon nanopipes

Measurements of liquid flow through single carbon nanopipes were first reported by Sinha et al., who fabricated 200–300 nm diameter carbon nanopipes in a porous alumina template using chemical vapor deposition [7]. The walls of the carbon nanopipes, although initially amorphous, were "graphitized" into structures that resembled multi-walled CNTs using a high-temperature annealing procedure. The average diameter of each carbon nanopipe, which varies from 10 to 20 percent along its axis, was measured using an environmental scanning electron microscope. Liquid flow through a carbon nanopipe was established by placing two liquid droplets with different diameters at opposite ends of it. The pressure gradient was calculated from the difference in the droplet diameters and the flow rate was evaluated by measuring the variation of the droplet diameters with time. The flow rates of glycerine through both amorphous and graphitized carbon nanopipes were consistent with predictions from the no-slip Poiseuille relation (i.e., $\varepsilon \approx 1$). Subsequent measurements by Ray et al., who used a syringe pump to drive water through 300–500 nm diameter carbon nanopipes fabricated using a similar procedure, are also consistent with the no-slip Poiseuille relation [1].

Whitby et al. measured water flow rates through an array of aligned carbon nanopipes with an average diameter of 44 nm [2]. The carbon nanopipe array was formed by coating the porous surface of an aluminium oxide template with layers of carbon *via* chemical vapor deposition. Unlike the carbon nanopipes of Sinha et al., the carbon nanopipes fabricated by Whitby et al. were not annealed and the carbon surface remained amorphous. The average inner diameter of the carbon nanopipes, which is controlled by the template pore size, was measured using transmission electron microscopy (TEM). A hydrostatic pressure difference was applied using a syringe pump and the flow rate was determined by

periodically weighing the water that exited the array. The water flow rate exceeded predictions from the no-slip Poiseuille relation with an enhancement factor of 22 and 34. From this enhancement data, as summarized in Table 1, Whitby et al. used Eq. (5) to calculate a slip length from 113 nm to 177 nm.

### 3.2. Water flow through carbon nanotubes

Experimental measurements of water flow through CNTs were first reported by Majumder et al., who examined pressure-driven flow through a membrane of open-ended and axially-aligned CNTs in a non-porous polymer matrix [3]. The CNT membrane was fabricated by spin-coating an aligned array of CNTs with a solution of polystyrene and toluene, followed by drying in a controlled environment to form a CNT/polystyrene composite system. Next, an $H_2O$ plasma-enhanced oxidation process was used to remove a thin layer of polystyrene from the membrane, opening the closed tips of the CNTs. The CNT density, based on analysis of scanning electron microscopy images, was estimated to be $6 \times 10^{10}$ tubes/cm$^2$ and the mean flow diameter of the CNTs was estimated to be 7 nm by measuring the ion permeability of the membrane [3,32]. The reported flow enhancement factor for the membrane, as summarized in Table 1, is between $10^4$ and $10^5$. The apparent slip length, calculated by solving Eq. (5) for $L_s$ using the measured enhancement factor, is between 3900 nm and 6800 nm. This slip length is much larger than the 10–100 nm slip length typically measured for hydrophobic surfaces and the 14–63 nm water/graphene slip length predicted from MD simulations [33].

Holt et al. report on measurements of water flow through a CNT membrane with a mean CNT diameter of 1.6 nm [4]. The membrane was formed by encapsulating an array of aligned CNTs in a hard silicon nitride matrix using low-pressure chemical vapor deposition. Excess silicon nitride was then removed from the membrane surface by ion milling and the ends of the CNTs were opened using reactive ion etching. The average CNT diameter was estimated using size-exclusion measurements and TEM image inspection. The pore density, also calculated from the TEM images, was $2.5 \times 10^{11}$ tubes/cm$^2$. As shown in Table 1, the calculated flow enhancement factor for water is between 560 and 9600 and the apparent slip length, calculated using Eq. (5), is from 140 nm to 1400 nm.

### 3.3. Discussion

Although the data from the experimental investigations suggest that liquid flow through sub-100 nm diameter carbon nanopipes and CNTs is enhanced, the magnitude of the enhancement and its variation with diameter—especially in CNTs with diameters smaller than 10 nm—is not clear. Surprisingly, the results of Majumder et al. compared to those of Holt et al. suggest that the flow enhancement increases by a factor of 10–100 as the mean CNT diameter is increased from 1.6 nm to 7 nm. The opposite trend is observed in larger carbon nanopipes, where the enhancement decreases with increasing diameter. Curvature-induced changes to the slip length, differences in CNT and carbon nanopipe internal surface structures, and changes in the liquid viscosity with CNT diameter have been suggested as mechanisms to explain the differences between the experimental reports [15]. Using MD simulation, we can examine the variation in flow enhancement with diameter systematically and investigate each of these mechanisms independently.

## 4. Molecular dynamics simulation of water inside CNTs

### 4.1. Introduction to MD simulation

The small length and time scales associated with molecular-level dynamics limit the ability of current laboratory experiments to resolve nanoscale transport phenomena. Molecular dynamics simulation, used in tandem with laboratory experiments, has become an effective tool for investigating molecular transport [34,35]. Molecular dynamics is a simulation technique that uses Newton's laws of motion to predict the position and momentum space trajectories of a system of classical particles. The only required inputs are intermolecular potential functions, which are used to calculate potential energies and forces, and an initial molecular configuration. The thermophysical properties of materials in the system and system-level transport properties can be found from the resulting kinematic trajectories and intermolecular forces.

Water–water, water–carbon, and carbon–carbon intermolecular potential functions must be specified in an MD simulation of a water/CNT system. In a typical water intermolecular potential function, the relative positions of the oxygen and hydrogen atoms correspond to known molecular structure data. Charged interaction sites are then placed around the atoms to reproduce the electrostatic multipoles of the molecule. The positions of the charged interactions sites and the form of the potential functions are tuned to reproduce experimentally-observed properties of bulk water and/or data from electronic structure calculations [36,37]. In simpler water models, such as TIP3P [38], TIP4P [39], TIP5P [36], and SPC [40], the positions of the atoms and the charge sites are fixed and the molecules interact as rigid objects. More sophisticated water models, such as Dang–Chang [41] and DPP [25], account for intra-molecular polarization. In these polarizable models, a computationally-intensive and iterative self-consistent field procedure must be used to evaluate the time dependence of the induced dipoles for each molecular configuration [41]. Since a typical MD simulation of water flow inside a CNT involves $10^3$ to $10^5$ water molecules and integrates the kinematic trajectories from 1 to 10 ns using a time step on the order of 1 fs (*e.g.* $10^6$–$10^7$ time-steps), only flow simulations involving rigid, non-polarizable water models are currently computationally tractable.

The interactions between the water molecules and the carbon surface are typically modeled using a Lennard–Jones (LJ) potential function between the carbon atoms and the oxygen atom of the water molecule. The LJ potential models short-range electron repulsion and long-range attractive dispersion interactions between atoms. Currently available LJ potential functions have been tuned to reproduce the experimentally-observed water/graphene contact angle [42] or data from electronic structure calculations [43]. More sophisticated potential functions that account for

**Table 1**
Experimentally measured flow enhancements and apparent water/carbon slip lengths [1–4]. The flow enhancement factor is calculated using Eq. (4) and the apparent slip length is calculated using Eq. (5).

| | Diameter (nm) | Enhancement, $\varepsilon$ | Apparent slip length, $L_s$ (nm) | |
|---|---|---|---|---|
| Carbon nanopipes | 300–500 | ≈1 | 0 | [Ref. 1] |
| | 44 | 22–34 | 113–177 | [Ref. 2] |
| Carbon nanotubes | 7 | $10^4$–$10^5$ | 3900–6800 | [Ref. 3] |
| | 1.6 | 560–9600 | 140–1400 | [Ref. 4] |

the polarization of the carbon atoms and electrostatic interactions between the water molecule dipole moment and the carbon atom quadrupole moment are under development [44].

The interactions between the carbon atoms can be modeled using a Tersoff [45] or Brenner potential function [46]. The potential parameters are tuned to reproduce the bond energies, bond lengths, and force constants of carbon-based molecules as measured from experiment or predicted from electronic structure calculations. To reduce the computational costs of the simulations, the carbon atoms in the majority of MD simulations of water flow through CNTs are fixed in space and a potential function is not implemented. This approximation is justified due to the high vibrational frequencies of carbon atoms in a CNT compared to those in liquid water [17]. When investigating thermal transport in water/CNT composite systems, however, the dynamics of the carbon atoms will be important [47,48].

Unless otherwise noted, the data in this report correspond to MD simulations performed in the *NVT* ensemble (constant mass, volume, and temperature) with a temperature maintained at 298 K using a Berendsen thermostat [49]. Water interactions are modeled using the non-polarizable TIP5P water model [36], water–carbon interactions are modeled using the LJ potential parameterized by Werder et al. [42], and the carbon atoms are fixed in space. The rotational dynamics of the water molecules are modeled using the quaternion method [50] and the translational dynamics are integrated using the Verlet leapfrog scheme with a 0.5 fs timestep [34].

### 4.2. Water structure near carbon surfaces

An important first step in predicting the mechanism of water flow through a CNT is to understand the intermolecular structure of the water molecules inside the tube. Surface force balance measurements of water squeezed between two mica sheets suggest that a transition from a disordered (bulk-like) liquid to an ordered (layer-like) liquid begins within 1 nm of a solid [51]. Consistent with this finding, data from neutron scattering experiments suggest that water inside a CNT forms an ordered molecular shell immediately adjacent to the CNT wall [52]. Experimental measurements of the water/carbon nanopipe contact angle, which is related to the wetting characteristics of the carbon surface and may be used to quantify the water/carbon potential energy [42], are available for tubes larger than 10 nm [53,54]. The variation in contact angle with diameter for smaller CNTs, where the effects of surface curvature on water/carbon interactions become relevant, is not yet available.

Molecular dynamics simulation has provided additional insight into the interaction between water molecules and carbon surfaces. Previous investigators, as summarized in the review article by Alexiadis and Kassinos [55], have used MD simulation to understand the interaction of water with a CNT surface and to explore how the density [56], structure [57], hydrogen-bonding characteristics [58], and free energy [59] vary with CNT diameter. In Fig. 2 we present a snapshot from one of our MD simulations of liquid water inside and outside a single-walled 10 nm diameter CNT. We superimpose on this snapshot the spatial variation in water density and hydrogen-bonding coordination number, as predicted from our simulations. Both inside and outside the CNT, water molecules far from the carbon surface do not interact directly with the solid, the water density is 1000 kg/m$^3$, and the water exhibits bulk-like hydrogen-bonding characteristics. Within 0.8 nm of the carbon surface, however, interactions with the solid influence the dynamics of the water molecules. The water density and coordination number within this interfacial region are spatially varying [16,56] and predictions from MD simulation indicate that transport properties in this region deviate from those of bulk water [60,61].

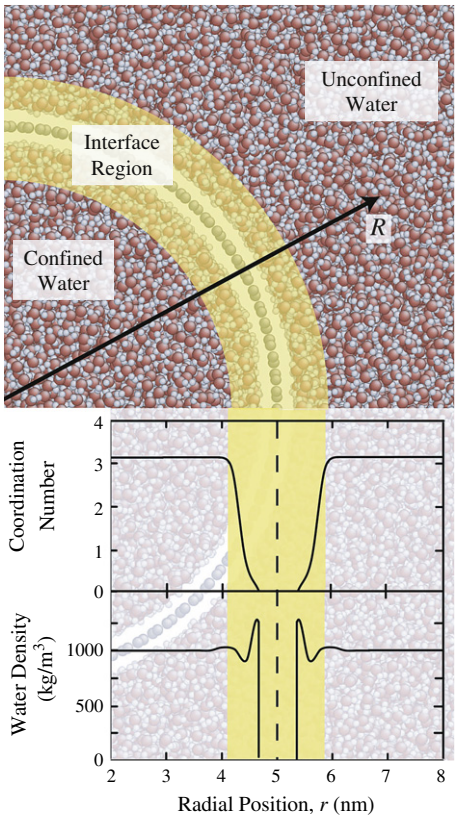


**Fig. 2.** Spatial variation in water density and hydrogen-bonding coordination number for water inside and outside a 10 nm diameter CNT. The highlighted interface region extends 0.8 nm from the carbon surface. For this CNT, the water recovers bulk-like properties beyond the interface region both inside and outside the CNT. Bulk-like properties are not recovered inside smaller diameter CNTs [57].

The water molecules immediately adjacent to the CNT surface form a high-density monolayer that interacts directly with the CNT surface. Using MD simulation, we previously examined how the structure of this monolayer varies with CNT diameter [57]. In Fig. 3(a)–(c) we present the position probability distributions, $P_r(\theta, z)$, of molecules in the monolayer near 6.93 nm, 2.76 nm, and 1.10 nm diameter CNTs. We find that in the monolayer inside a 10.4 nm CNT (not shown), molecules near the interior interface assume a distribution indistinguishable from that outside the CNTs. This behavior suggests that the effects of carbon surface curvature on the behavior of water molecules near the CNT surface are negligible in tubes with diameters larger than 10 nm. The mass distribution inside the 6.93 nm diameter CNT is also correlated to the CNT surface structure, although the patterning is less prevalent than that outside the CNT. Inside the 2.76 nm CNT, density enhancements are present within some of the potential wells formed by the carbon honeycombs, while other potential wells remain statistically unfilled. Finally, inside the 1.10 nm CNT, the molecular positions are completely uncorrelated to the carbon structure. As we will discuss below, this decoupling between the water structure and the CNT surface structure leads to changes in the water/CNT slip length with decreasing CNT diameter.

## 5. MD simulation of water flow through CNTs

### 5.1. Flow simulations

In addition to examining the structure of water molecules near carbon surfaces, MD simulation can be used to explore the variation in flow enhancement with CNT diameter. Results from previous MD

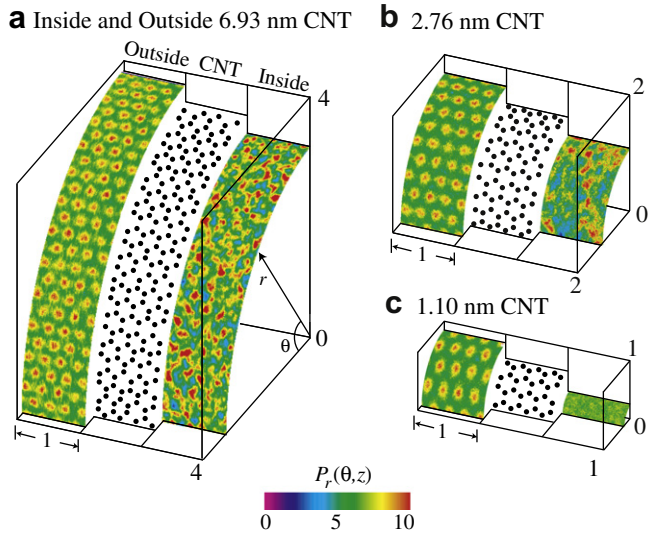


**Fig. 3.** Molecular distribution in the outside and inside monolayers for (a) 6.93 nm, (b) 2.76 nm, and (c) 1.10 nm diameter CNTs. All dimensions are given in nanometers. The distribution in the outside monolayer is unaffected by surface curvature. The distribution in the inside monolayer becomes more uniform with decreasing CNT diameter, which indicates a decoupling between the liquid structure and the solid surface. The distribution in the inside monolayer for CNTs larger than approximately 7 nm is unaffected by surface curvature [57].

simulations of water [56], simple liquids [18], and two-phase water/gas flows [28] through CNTs indicate that the flow is governed by slip at the solid boundary. In these previous investigations, flow was established by either applying an external force field (*e.g.*, gravity-driven flow [62]) or pushing water molecules inside the tube using a piston-like mechanism [56]. To calculate the flow enhancement, however, the axial pressure gradient must be specified. This information is absent from many previous reports and, as a result, the flow enhancement factor cannot be calculated.

In Fig. 4, we present the relationship between volumetric flow rate and pressure gradient for CNTs with diameters between 1.66 nm and 6.93 nm, as calculated in our previous report [19] and obtained from more recent simulations. Each CNT contains between 3100 and 12,220 water molecules, corresponding to tube lengths that vary from 80 nm (for the 1.66 nm diameter CNT) to 11 nm (for the 6.93 nm diameter CNT). Periodic boundary conditions are applied in the flow direction and a pressure gradient is induced (i.e. flow) using a reflecting particle membrane [23]. We calculate $\partial P/\partial z$ by evaluating the pressure within several subvolumes along the tube axis and performing a linear regression analysis. Since we know the position and momentum of each particle in the simulation, the radial velocity profile can be calculated directly. The volumetric flow rate through the CNT is then obtained by integrating the radial velocity profile [19,23].

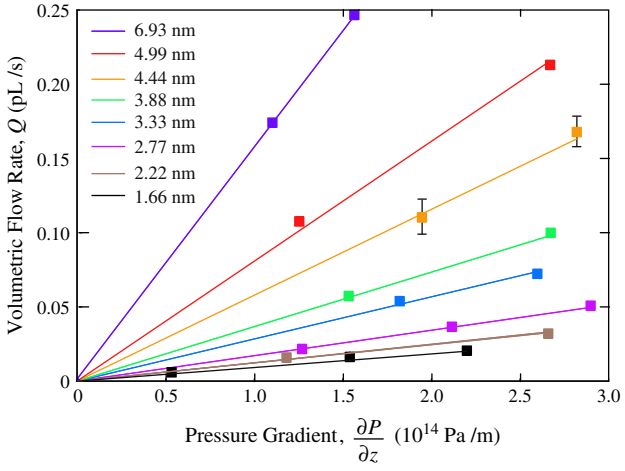


**Fig. 4.** Volumetric flow rate in CNTs versus pressure gradient. Over the pressure range investigated, $Q$ is proportional to $\partial P/\partial z$. Consistent with Poiseuille flow, the volumetric flow rate increases monotonically with CNT diameter for a fixed pressure gradient. Error bars, as shown for the 4.44 nm diameter CNT, are similar for all points.

In Fig. 5 we present the flow enhancement factor (measured flow rate divided by that predicted from the no-slip Poiseuille relation) versus tube diameter for CNTs with diameters ranging from 1.66 nm to 6.93 nm. Consistent with previous experimental reports, the cross-sectional flow area is evaluating using the full CNT diameter [19]. The magnitude of the flow enhancement predicted from MD simulation decreases monotonically with increasing CNT diameter. This finding is opposite to the experimental results of Majumder et al. compared with those of Holt et al., which suggest that the flow enhancement increases by a factor of 10–100 as the mean CNT diameter is increased from 1.6 nm to 7 nm.

Simulating pressure-driven water flow through CNTs with diameters larger than 6.93 nm is computationally expensive and was not done. Molecular dynamics simulation can, however, be used to predict the variation of water viscosity and slip length with CNT diameter. The results will allow us to calculate, using Eq. (6), the variation in flow enhancement with diameter for larger CNTs. We will use the results to (i) determine if water flow through the CNTs is consistent with predictions from the slip-modified Poiseuille flow, and (ii) explore the asymptotic transition from enhanced flow to no-slip Poiseuille flow with increasing diameter.

### 5.2. Water viscosity

We predict the water viscosity inside each CNT from the axial self-diffusion coefficient, $D_{zz}$, which is related to the viscosity *via* the Einstein relation [63]:

$$\mu = \frac{k_B T}{3\pi a} \frac{1}{D_{zz}}. \tag{7}$$

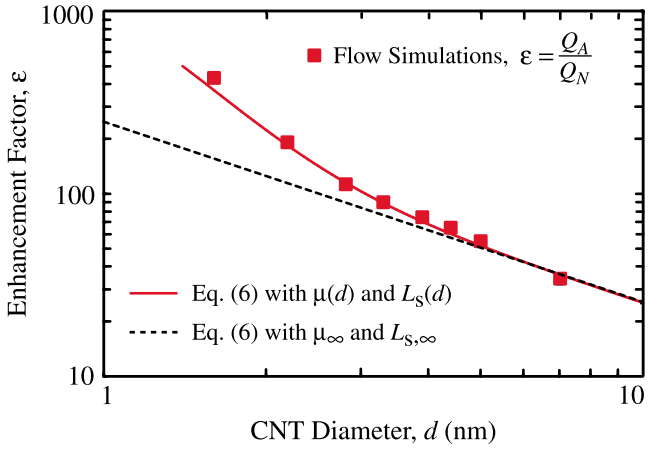


**Fig. 5.** Variation in flow enhancement factor with CNT diameter, as predicted from MD simulation. We estimate the uncertainty in the enhancement predicted directly from the flow simulations (solid squares), which arises primarily from specifying the pressure gradient, to be ±20%. The uncertainty in the enhancement calculated using Eq. (6) (solid line), which arises from predicting the water viscosity, is ±15%. For comparison purposes, we also plot the enhancement corresponding to a bulk viscosity and our predicted slip length for water over a flat graphene sheet ($L_s = 30$ nm; see Section 5.3).

In Eq. (7), $k_B$ is the Boltzmann constant and $a$ is an effective molecular diameter taken to be 0.17 nm [64]. The axial self-diffusion coefficient can be predicted from MD simulation using a Green–Kubo linear response relation or by tracking the mean-squared displacement of the water molecules in an equilibrium (no net flow) simulation [34]. For the data presented here, we calculated $D_{zz}$ by tracking the mean-squared axial displacement of the water molecules.

The water viscosity, as presented in Fig. 6(a), increases monotonically with increasing CNT diameter. As the CNT diameter increases beyond the sizes that we examined, we expect that the water viscosity inside the tube will converge to the value we predict for bulk water ($\mu_\infty = 1.03 \times 10^{-3}$ Pa s). Inside smaller CNTs, the effective water viscosity is smaller due to the increased ratio of interface to bulk-like area [65]. This behavior led us to define a weighted-average expression for the effective water viscosity [19]:

$$\mu(d) = \mu_i \frac{A_i}{A_t} + \mu_\infty \left(1 - \frac{A_i}{A_t}\right), \tag{8}$$

where $\mu_i$ is the viscosity of the interface region, $\mu_\infty$ is the viscosity of bulk water, $A_i$ is the interface area (see Fig. 2), and $A_t$ is the total cross-sectional flow area.

We define the interface area to be the annular region within 0.8 nm of the CNT surface and set $\mu_i$ equal to the viscosity inside the 1.66 nm diameter CNT, where the interface region covers 97% of the cross-sectional area. Equation (8), which is superimposed on the data in Fig. 6(a), predicts that the effective water viscosity inside the CNT will be within 10% of the bulk value when the tube diameter is larger than 10 nm. Equation (8) will not accurately predict the water viscosity in CNTs with diameters smaller than 1.6 nm, where momentum transport will be related to the intermolecular structure [9,24,26].

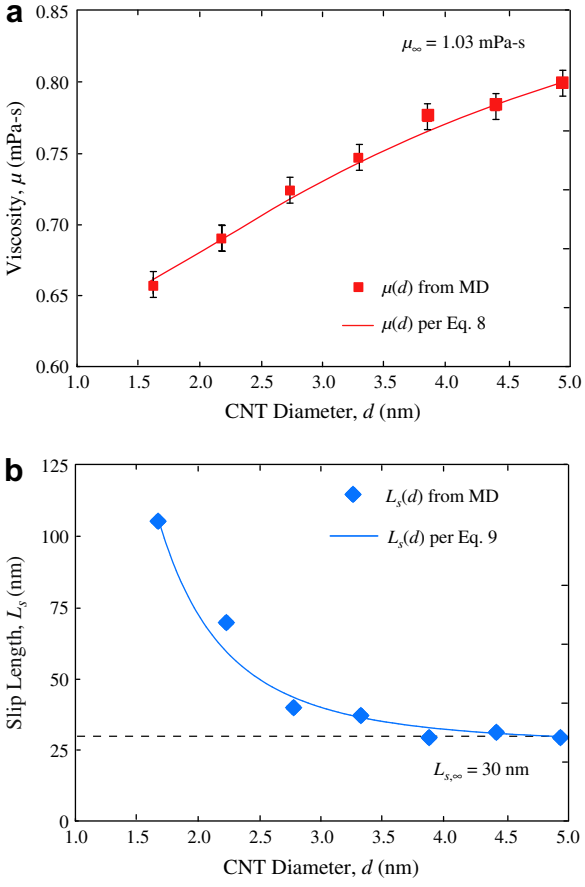


**Fig. 6.** (a) Variation of water viscosity with CNT diameter. The MD viscosity was predicted from equilibrium simulation using Eq. (7). (b) Variation of water/CNT slip length with CNT diameter. The MD slip length was evaluated from the velocity profile inside each CNT and Eq. (2). The variation in slip length with CNT diameter is fit using Eq. (9) and the dashed horizontal line identifies $L_{s,\infty}$(=30 nm). The uncertainty in the slip length is ×1 nm, making the error bars smaller than the data points.

### 5.3. Water/CNT slip length

The apparent water/CNT slip lengths calculated from the experimental flow data, as presented in Table 1, are found by solving Eq. (5) for $L_s$ using the measured flow enhancement. This procedure miscalculates the actual slip length because the confinement-induced changes to the liquid viscosity discussed in Section 5.2 are neglected. Miscalculated slip lengths will also occur if the available membrane flow area (used to calculate $Q_N$) is incorrectly measured.

In an MD simulation, where we know the positions and velocities of every molecule, we can predict the radial velocity profile and calculate the slip length directly using Eq. (2). In Fig. 6(b), we present the variation in the water/CNT slip length with CNT diameter directly, as predicted from MD simulation. The water/carbon slip length decreases monotonically with increasing CNT diameter and converges to a value of $30 \pm 1$ nm for CNTs with diameters larger than 5 nm. As discussed in Section 4.2, the effect of surface curvature on the potential energy landscape becomes negligible as the CNT diameter is increased beyond 7 nm [57]. This trend explains why the slip length converges to 30 nm—the same slip length we predict for water near a flat graphene sheet [19]—with increasing CNT diameter. We find that the variation in slip length with CNT diameter, as shown in Fig. 6(b), can be described by the empirical relation

$$L_s(d) = L_{s,\infty} + \frac{C}{d^3}, \tag{9}$$

where $L_{s,\infty}$(= 30 nm) is the slip length over a flat graphene sheet and $C$(= 352 nm$^4$) is a fitting parameter.

Liquid slip at a solid/liquid boundary is a rate process limited by the ability of molecules to hop between open surface lattice sites [66]. The slip length is therefore large when the solid/liquid binding energy is weak and the solid/liquid potential energy landscape near the solid surface is smooth. As discussed in Section 4.2, decreasing the CNT diameter weakens the coupling between the water monolayer and the carbon surface. At a given time, fewer of the low-energy potential wells formed by the carbon surface will be filled compared to a lager diameter CNT [57]. We attribute the increase in slip length with decreasing CNT diameter to this behavior.

### 5.4. Flow enhancement

Substituting the expressions for $\mu(d)$ [Eq. (8)] and $L_s(d)$ [Eq. (9)] into Eq. (6) gives a model, based on the Poiseuille flow relation, that can be used to predict the variation in flow enhancement with CNT diameter. The predictions from this model are superimposed on the flow enhancements calculated from the pressure-driven flow simulations in Fig. 5. The good agreement between the enhancement model and the enhancements we calculated directly from MD simulation indicates that a Poiseuille description of flow is valid in CNTs with diameters as small as 1.66 nm.

As summarized in Table 2, the results from our MD simulations suggest four regimes of water flow inside CNTs. In CNTs with

**Table 2**
Regimes of water flow through CNTs, as predicted from MD simulation.

| Diameter, $d$ (nm) | Enhancement, $\varepsilon$ | Enhancement magnitude |
|---|---|---|
| <1.6 | Subcontinuum flow | Varies with liquid structure |
| 1.6–5 | $(1+8L_S/d)\mu_\infty/\mu(d)$ | ~500 |
| 5–10 | $(1+8L_{S,\infty}/d)\mu_\infty/\mu(d)$ | ~100 |
| >10 | $(1+8L_{S,\infty}/d)$ | 1–10 |

diameters smaller than about 1.6 nm, the interface region spans the entire cross-sectional flow area and a continuum description of the fluid is invalid. As reported by us and others [9,26,67], the flow characteristics are related to the liquid's intermolecular structure. The movement of individual molecules must be considered when modeling transport through the tube. In CNTs with diameters between 1.6 nm and 5 nm, a continuum description of the fluid is valid but diameter-related changes to the slip length and the viscosity must be considered when predicting the flow enhancement. When the CNT diameter is between 5 nm and 10 nm, confinement-related changes to the water viscosity must be considered and the slip length will be close to the flat sheet limit. Finally, in CNTs with diameter larger than 10 nm, diameter-related changes in the water viscosity are negligible and the slip length will be equal to the flat sheet limit. The flow enhancement will then decrease with increasing CNT diameter until $L_S \ll D$, when the flow rate becomes consistent with predictions from the no-slip Poiseuille relation.

In addition to the results presented here, Joseph and Aluru used MD simulation to investigate gravity-driven water flow through a 2.22 nm diameter CNT [17]. Using a cross-sectional flow area definition consistent with that used here, we calculate a flow enhancement factor of 459 from their data. We believe that the difference between this value and our result (184) for the same tube is due to differences in the potential functions used to model the molecular interactions. The water–carbon LJ potential function used by Joseph and Aluru predicts a weaker water/carbon interaction energy than the potential used here. This difference will increase the slip length in their flow simulations, leading to a larger flow enhancement. Additionally, Joseph and Aluru used the SPC/E rigid water potential function, which will lead to a different water viscosity.

The comparison between our simulation data and that reported by Joseph and Aluru illustrates the sensitivity of MD predictions to the chosen intermolecular potential functions. As discussed by Koumoutsakos et al., increasing the magnitude of the water/carbon LJ interaction energy by 50 and 100 percent decreases the water/carbon slip length by factors of two and four [33]. Likewise, depending on the choice of water model, the bulk water viscosity predicted from MD at a temperature of 298 K varies from 0.6 to 1.0 mPa s [64]. These differences impede a direct comparison between MD simulations performed using different interatomic potentials and make quantitative comparisons to experimental data difficult. When using the same set of parameters to systematically investigate a range of systems, however, MD simulation can effectively elucidate changes in system-level transport and deviations from continuum mechanics [68]. Improvements to intermolecular potential functions, especially the water/carbon potential function, will enable a more quantitative comparison between simulation and experiment.

## 6. Comparison between experiment and simulation

Our MD-predicted enhancement for the 1.66 nm diameter CNT is near the lower end of the 560–9600 enhancement range measured by Holt et al. for a membrane of CNTs with a mean diameter of 1.6 nm. Since the water intermolecular orientations in a 1.6 nm diameter CNTs are uncorrelated [26], the net electric field in each region of space is close to zero and the effects of molecular polarizability on flow should be negligible. We therefore do not expect that simulations using more sophisticated water models will predict significantly different flow enhancements. However, possible variations in the water-CNT interaction with tube diameter—not described accurately using currently available LJ potential parameterizations—may account for some of the discrepancy. We also note that the calculated flow enhancement is sensitive to the CNT diameter. For example, a 0.1 nm mismeasurement of the mean CNT radius (used to calculate $Q_N$ in Eq. (4)) will alter the experimentally measured enhancement range for the membrane of Holt et al. by 30%.

The predictions from our MD simulations do not support the $10^4$–$10^5$ enhancement measurements of Majumder et al. for a membrane of 7 nm diameter CNTs. Our results suggest an enhancement factor of only 32 for such CNTs. Some discrepancy may arise from differences in CNT surface chemistry/structure or limitations in the MD potential functions. The exceptionally large flow enhancement reported by Majumder et al., however, suggest to us a miscalculation of either the mean CNT diameter or the density of open-ended CNTs in their membrane. As discussed in Section 3, Majumder et al. estimate the diameter of the CNT pores by measuring the diffusion rate of ions through the membrane. The non-uniform electric field near the open end of a CNT, however, will limit the ability for ions to enter the tube while allowing water molecules to pass freely [69]. If this restriction on ion entrance is not considered, the apparent diameter calculated from the ion diffusion rates will be smaller than the flow diameter available for water molecules. This diameter discrepancy would cause the calculated water flow enhancement to exceed the actual flow enhancement.

The apparent slip length calculated by Whitby et al. for 44 nm diameter carbon nanopipes is from 110 nm to 220 nm, which is larger than the value of 30 nm we have predicted directly from MD simulation. Unlike like the graphitic CNTs investigated in our MD simulation, however, the walls of the 44 nm diameter carbon nanopipes are multi-layered and amorphous. Since the structure of the carbon surface has a pronounced effect on the water/carbon contact angle [53], changes in the water/carbon slip length with surface structure are also expected. Additionally, the LJ water–carbon potential function used in our MD simulation was parameterized to reproduce the wetting characteristics of water on a flat graphitic surface. Variations in the carbon atom electrostatic multipoles (caused by the non-uniform distribution of carbon atoms) will not be captured using current potential functions and may affect transport through the nanopipe.

An additional factor that may influence water transport through 44 nm diameter carbon nanopipes is the Fakier effect, where water only interacts with the asperities along the carbon surface and does not fully penetrate through the surface roughness [70]. The Fakier effect reduces the liquid–solid contact area, causing a decrease in the flow friction (relative to Poiseuille flow), and an increase in the apparent liquid slippage. For water flow over rough surfaces, the Fakier effect has been experimentally shown to increase the apparent slip length by one order of magnitude [70]. Flow enhancement may also be caused by air entrainment, where a low-viscosity gaseous layer near the solid surface entrains the liquid and increases the mean flow velocity. For example, the apparent slip length in water-filled 300–500 nm diameter carbon nanopipes is approximately zero [1]. Entrainment, however, can increase the apparent water/carbon slip length to the order of 100 nm [1].

For CNTs with diameter larger than 200 nm, predictions from MD simulation suggest that the effects of liquid slip are negligible

and the viscosity of the liquid will be equal to that of the bulk liquid. This conclusion is consistent with measurements of water and glycerine flow through similarly sized carbon nanopipes, which are inline with predictions from the no-slip Poiseuille relation [1,7]. Depending on the scale of the carbon nanopipe surface roughness, however, the Fakier effect and air entrainment are possible mechanisms by which the flow rate through these larger carbon nanopipes could be enhanced.

## 7. Conclusion and outlook

In parallel with experimental investigations, MD simulation can be an effective tool for investigating the behavior of water near carbon surfaces and exploring the nature of water flow through CNTs and carbon nanopipes. Predictions from MD simulation indicate that (i) a continuum description of water flow is appropriate inside CNTs larger than 1.66 nm, (ii) diameter-related changes to the viscosity and slip length must be considered when modeling liquid flow, and (iii) the flow enhancement factor decreases monotonically with increasing diameter for smooth walled tubes. The variation in flow enhancement predicted using MD is qualitatively consistent with the majority of the experimental data. Since the MD simulations considered flow though atomically smooth and defect-free CNTs, discrepancies between simulation and experiment are likely caused by differences in the structure and/or chemistry of the carbon surface.

Additional measurements of water flow through CNTs and carbon nanopipes are required to further understand the magnitude of the flow enhancement and its variation with CNT diameter. Better characterization of CNT and carbon nanopipe surfaces will also help to elucidate the effects of surface structure and surface chemistry on flow. Physically accurate potential functions and simulations utilizing more sophisticated water models are also needed to more fully understand the mechanisms of water flow through smaller CNTs. These additional insights into the physics of nanoscale flows, coupled with new device fabrication processes, will be central to the design and optimization of next-generation nanofluidic devices.

## References

[1] S.S. Ray, P. Chando, A.L. Yarin, Enhanced release of liquid from carbon nanotubes due to entrainment by an air layer, Nanotechnology 20 (2009) 095711.
[2] M. Whitby, L. Cagnon, M. Thanou, N. Quirke, Enhanced fluid flow through nanoscale carbon pipes, Nano Letters 8 (2008) 2632–2637 and corresponding erratum which corrects the reported water/carbon nanotube slip length.
[3] M. Majumder, N. Chopra, R. Andrews, B.J. Hinds, Nanoscale hydrodynamics: enhanced flow in carbon nanotubes, Nature 438 (2005) 44.
[4] J.K. Holt, H.G. Park, Y. Wang, M. Stadermann, A.B. Artyukhin, C.P. Grigoropoulos, A. Noy, O. Bakajin, Fast mass transport through sub-2-nanometer carbon nanotubes, Science 312 (2006) 1034–1037.
[5] T. Yamada, T. Namai, K. Hata, D.N. Futaba, K. Mizuno, J. Fan, M. Yudasaka, M. Yumura, S. Iigima, Size-selective growth of double-walled carbon nanotube forests from engineered iron catalysts, Nature Nanotechnology 1 (2006) 131–136.
[6] M. Whitby, N. Quirke, Fluid flow in carbon nanotubes and nanopipes, Nature Nanotechnology 2 (2007) 87–94.
[7] S. Sinha, M.P. Rossi, D. Mattia, Y. Gogotsi, H.H. Bau, Induction and measurement of minute flow rates through nanopipes, Physics of Fluids 19 (2007) 013603.
[8] Y. Yun, Z. Dong, V.N. Shanov, A. Bange, W.R. Heineman, H.B. Halsall, L. Conforti, A. Bhattacharya, M.J. Schulz, On-line carbon nanotube-based biosensors in microfluidic channels, Proceedings of the Society of Photographic Instrumentation Engineers 6528 (2007) 65280T.
[9] B. Corry, Designing carbon nanotube membranes for efficient water desalination, Journal of Physical Chemistry B 112 (2008) 1427–1434.
[10] A. Kalra, S. Garde, G. Hummer, Osmotic water transport through carbon nanotube membranes, Proceedings of the National Academy of Sciences of the United States of America 100 (2003) 10175–10180.
[11] D.S. Sholl, J.K. Johnson, Making high-flux membranes with carbon nanotubes, Science 312 (2006) 1003–1004.
[12] V.V. Simonyan, J.K. Johnson, Hydrogen storage in carbon nanotubes and graphitic nanofibers, Journal of Alloys and Compounds 330–332 (2002) 659–665.
[13] M.G. Schrlau, N.J. Dun, H.H. Bau, Cell electrophysiology with carbon nanopipettes, ACS Nano 3 (2009) 563–568.
[14] A.I. Skoulidas, D.S. Sholl, J.K. Johnson, Adsorption and diffusion of carbon dioxide and nitrogen through single-walled carbon nanotube membranes, Journal of Chemical Physics 124 (2006) 054708.
[15] H. Verweij, M.C. Schillo, J. Li, Fast mass transport through carbon nanotube membranes, Small 3 (2007) 1996–2004.
[16] E.M. Kotsalis, J.H. Walther, P. Koumoutsakos, Multiphase water flow inside carbon nanotubes, International Journal of Multiphase Flow 30 (2004) 995–1010.
[17] S. Joseph, N.R. Aluru, Why are carbon nanotubes fast transporters of water? Nano Letters 8 (2008) 452–458.
[18] V.P. Sokhan, D. Nicholson, N. Quirke, Fluid flow in nanopores: accurate boundary conditions for carbon nanotubes, Journal of Chemical Physics 117 (2002) 8531–8539.
[19] J.A. Thomas, A.J.H. McGaughey, Reassessing fast water transport through carbon nanotubes, Nano Letters 9 (2008) 2788–2793.
[20] P. Joseph, P. Tabeling, Direct measurement of the apparent slip length, Physical Review E 71 (2005) 035303R.
[21] J.-L. Barrat, F. Chiaruttini, Kapitza resistance at the liquid–solid interface, Molecular Physics 101 (2003) 1605–1610.
[22] K.P. Travis, B.D. Todd, D.J. Evans, Departure from Navier–Stokes hydrodynamics in confined liquids, Physical Review E 55 (1997) 4288–4295.
[23] J. Li, D. Liao, S. Yip, Coupling continuum to molecular-dynamics simulation: reflecting particle method and the field estimator, Physical Review E 57 (1998) 7259–7267.
[24] G. Hummer, J.C. Rasaiah, J.P. Noworyta, Water conduction through the hydrophobic channel of a carbon nanotube, Nature 414 (2001) 188–190.
[25] A. Striolo, The mechanism of water diffusion in narrow carbon nanotubes, Nano Letters 6 (2006) 633–639.
[26] J.A. Thomas, A.J.H. McGaughey, Water flow in carbon nanotubes: transition to subcontinuum transport, Physical Review Letters 102 (2009) 184502.
[27] J. Berthier, P. Silberzan, Microfluidics for Biotechnology, Artech House, Norwood, MA, 2006.
[28] S.C. Kassinos, J.H. Walther, E.M. Kotsalis, P. Koumoutsakos, Flow of aqueous solutions in carbon nanotubes, in: S. Attinger, P. Koumoutsakos (Eds.), Multiscale Modeling and Simulation, Springer, 2004, pp. 220–224.
[29] F. White, Viscous Fluid Flow, third ed. McGraw-Hill, Boston, 2006.
[30] J.S. Hansen, P.J. Daivis, K.P. Travis, B.D. Todd, Parameterization of the non-local viscosity kernel for an atomic fluid, Physical Review E 76 (2007) 041121.
[31] T. Ohara, D. Suzuki, Intermolecular momentum transfers in a simple liquid and its contribution to shear viscosity, Microscale Thermophysical Engineering 5 (2001) 117–130.
[32] B.J. Hinds, N. Chopra, T. Rantell, R. Andrews, V. Gavalas, L.G. Bachas, Aligned multi-walled carbon nanotube membranes, Science 303 (2004) 62–65.
[33] P. Koumoutsakos, R.L. Jaffe, T. Werder, J.H. Walther, On the validity of the no-slip condition in nanofluidics, Nanotechnology 1 (2003) 148–151.
[34] M.P. Allen, D.J. Tildesley, Computer Simulation of Liquids, Clarendon Press, Oxford, 1987.
[35] D.C. Rapaport, The Art of Molecular Dynamics Simulation, Cambridge University Press, Cambridge, 2004.
[36] M.W. Mahoney, W.L. Jorgensen, A five-site model for liquid water and the reproduction of the density anomaly by rigid, non-polarizable potential functions, Journal of Chemical Physics 112 (2000) 8910–8922.
[37] A. DeFusco, D.P. Schofield, K.D. Jordan, Comparison of models with distributed polarizable sites for describing water custers, Molecular Physics 105 (2007) 2681–2696.
[38] W.L. Jorgensen, J. Chandrasekhar, J. Madura, R.W. Impey, M.L. Klein, Comparison of simple potential functions for simulating liquid water, Journal of Chemical Physics 79 (1983) 926–935.
[39] W.L. Jorgensen, J.D. Madura, Temperature and size dependence for Monte Carlo simulations of TIP4P water, Molecular Physics 56 (1985) 1381–1392.
[40] H.J.C. Berendsen, J.P.M. Postma, W.F. van Gunsteren, J. Hermans, B. Pullman, Intermolecular Forces, Reidel, Dordrecht, 1981.
[41] L.X. Dang, T.-M. Chang, Molecular dynamics study of water clusters, liquid, and liquid–vapor interface of water with many-body potentials, Journal of Chemical Physics 106 (1997) 8149–8159.
[42] T. Werder, J.H. Walther, R.L. Jaffe, T. Halicioglu, P. Koumoutsakos, On the water–carbon interaction for use in molecular dynamics simulations of graphite and carbon nanotubes, Journal of Physical Chemistry B 107 (2003) 1345–1352.
[43] A. Pertsina, M. Grunze, Water as a lubricant for graphite: a computer simulation study, Journal of Chemical Physics 125 (2006) 114707.
[44] G. Jenness, K.D. Jordan, A DF-DFT-SAPT investigation of the binding of water of coronene and dodecabenzocoronene: implications for the water–graphite interaction, Journal of Physical Chemistry C 113 (2009) 10242–10248.
[45] J. Tersoff, Empirical interatomic potential for carbon, with applications to amorphous carbon, Physical Review Letters 61 (1988) 2879–2882.
[46] D.W. Brenner, O.A. Shenderova, J.A. Harrison, S.J. Stuart, B. Ni, S.B. Sinnott, A second-generation reactive empirical bond order (REBO) potential energy expression for hydrocarbons, Journal of Physics: Condensed Matter 14 (2002) 783–802.

[47] J. Shiomi, S. Maruyama, Water transport inside a single-walled carbon nanotube driven by a temperature gradient, Nanotechnology 20 (2009) 055708.
[48] M.J. Longhurst, N. Quirke, Temperature-driven pumping of fluid through single-walled carbon nanotubes, Nano Letters 7 (2007) 3324–3328.
[49] H.J.C. Berendsen, J.P.M. Postma, W.F. van Gunsteren, A. DiNola, J.R. Haak, Molecular dynamics with coupling to an external bath, Journal of Chemical Physics 81 (1984) 3684–3690.
[50] C.F.F. Karney, Quaternions in molecular modeling, Journal of Molecular Graphics and Modelling 25 (2007) 595–604.
[51] U. Raviv, J. Klein, Fluidity of bound hydration layers, Science 297 (2002) 1540–1543.
[52] E. Mamontov, C.J. Burnham, S.-H. Chen, A.P. Moravsky, C.-K. Loong, N.R. de Souza, A.I. Kolesnikov, Dynamics of water confined in single- and double-wall carbon nanotubes, The Journal of Chemical Physics 124 (2006) 194703.
[53] D. Mattia, M.P. Rossi, B.M. Kim, G. Korneva, H.H. Bau, Y. Gogotsi, Effect of graphitization on the wettability and electrical conductivity of CVD-Carbon Nanotubes and Films, Journal of Chemical Physics B 110 (2006) 9850–9855.
[54] A.H. Barber, S.R. Cohen, H.D. Wagner, External and internal wetting of carbon nanotubes with organic liquids, Physical Review B 71 (2005) 115443.
[55] A. Alexiadis, S. Kassinos, Molecular simulation of water in carbon nanotubes, Chemical Reviews 108 (2008) 5014–5034.
[56] I. Hanasaki, A. Nakatani, Flow structure of water in carbon nanotubes: Poiseuille type or plug-like? Journal of Chemical Physics 124 (2006) 144708.
[57] J.A. Thomas, A.J.H. McGaughey, Density, distribution, and orientation of water molecules inside and outside carbon nanotubes, Journal of Chemical Physics 128 (2008) 084715.
[58] J. Martí, M.C. Gordillo, Temperature effects on the static and dynamic properties of liquid water inside nanotubes, Physical Review E 64 (2001) 021504.
[59] W. Waghe, J.C. Rasaiah, G. Hummer, Filling and emptying kinetics of carbon nanotubes in water, Journal of Chemical Physics 117 (2002) 10789–10795.
[60] N. Choudhury, Dynamics of water in solvation shells and intersolute regions of C60: a molecular dynamics simulation study, Journal of Physical Chemistry C 111 (2007) 2565–2572.
[61] J.A. Thomas, A.J.H. McGaughey, Effect of surface wettability on liquid density, structure, and diffusion near a solid surface, Journal of Chemical Physics 126 (2007) 034707.
[62] J. Koplik, J.R. Banavar, J.F. Willemsen, Molecular dynamics of Poiseuille flow and moving contact lines, Physical Review Letters 60 (1988) 1282–1285.
[63] D.A. McQuarrie, Statistical Mechanics, Viva Books Private Limited, New Delhi, 2005.
[64] S. Yongli, S. Minhua, C. Weidong, M. Congxiao, L. Fang, The examination of water potentials by simulating viscosity, Computational Materials Science 38 (2007) 737–740.
[65] U. Raviv, S. Perkin, P. Laurat, J. Klein, Fluidity of water confined down to subnanometer films, Langmuir 20 (2004) 5322–5332.
[66] S. Lichter, A. Martini, R.Q. Snurr, Q. Wang, Liquid slip in nanoscale channels as a rate process, Physical Review Letters 98 (2007) 226001.
[67] S. Joseph, N.R. Aluru, Pumping of confined water in carbon nanotubes by rotation–translation coupling, Physical Review Letters 101 (2008) 064502.
[68] E.S. Landry, S. Mikkilineni, M. Paharia, A.J.H. McGaughey, Droplet evaporation: a molecular dynamics investigation, Journal of Applied Physics 102 (2007) 124301.
[69] F. Fornasiero, H.G. Park, J.K. Holt, M. Stadermann, C.P. Grigoropoulos, A. Noy, O. Bakajin, Ion exclusion by sub-2-nm carbon nanotube pores, Proceedings of the National Academy of Sciences of the United States of America 45 (2008) 17250–17255.
[70] P. Joseph, C. Cottin-Bizonne, J.-M. Benoit, C. Ybert, C. Journet, P. Tabeling, L. Bocquet, Slippage of water past superhydrophobic carbon nanotube forests in microchannels, Physical Review Letters 97 (2006) 156104.